

Infrared lines as probes of solar magnetic features

XIII. The relative flux in weak and strong quiet-sun magnetic fields

N. Meunier¹, S.K. Solanki², and W.C. Livingston³

¹ URA 2080 CNRS, DASOP, Observatoire de Paris, 5 Place Janssen, F-92195 Meudon, France

² Institute of Astronomy, ETH-Zentrum, CH-8092 Zürich, Switzerland

³ National Solar Observatory, NOAO, P.O. Box 26732, Tucson, AZ 85726, USA

Received 29 May 1997 / Accepted 11 August 1997

Abstract. An estimate of the fraction of magnetic flux in intrinsically weak-field form, i.e. fields with less than 1 kG intrinsic strength, in the quiet Sun is presented. We find that on average approximately 2/3 of the flux is in weak-field form, although our data allow a range of values between 25% and 85%. These estimates have been derived with the help of radiative transfer model calculations from low-noise scans through the quiet Sun at fixed wavelengths within a Zeeman sensitive spectral line at 1.56 μm . They represent the first rapidly modulated polarimetric observations of solar 1.56 μm radiation. These scans show that the polarimetric signature near the core of the line exhibits a very different spatial structure than in the outer line wings. Since the outer part of the line profile is only sensitive to intrinsically strong magnetic fields, while the central part reacts also to intrinsically weak fields, this implies that intrinsically weak fields are distributed differently on the surface than strong fields are (weak-field features lie closer together). The spatial distribution suggests that the strong fields we are observing are network elements, whereas the weak fields are intranetwork features.

Further results, such as the average distance between weak and strong field features, flux distribution, spatial power spectra and the Stokes asymmetry of intrinsically weak fields are also presented. In particular, we find that the flux per magnetic feature is distributed lognormally, in agreement with a similar finding for sunspot umbral areas by Bogdan et al. (1988).

Key words: Sun: magnetic fields – Sun: infrared – polarization

1. Introduction

The magnetic field of the Sun underlies a whole range of phenomena, from sunspots to the heating and structuring of the solar corona. In the last two decades, the study of solar magnetism has concentrated on the strong-field component, described by

Send offprint requests to: N. Meunier

flux tubes with field strengths of 1–3 kG in their photospheric layers (see Spruit & Roberts 1983; Stenflo 1989; Thomas & Weiss 1992; Solanki 1993 for reviews). In the photosphere the magnetic energy density in these fields, $B^2/8\pi$, is on the order of the gas pressure and an order of magnitude larger than the kinetic energy density of convection. Such fields are also referred to as kG or intrinsically strong fields. They dominate within active regions and in the network.

There is, however, increasing evidence for a component of the field that is intrinsically weak, i.e. whose field strength is well below 1 kG in the mid-photospheric layers (Tarbell et al. 1979; Stenflo 1982; Rüedi et al. 1992; Faurobert-Scholl 1993; Keller et al. 1994; Lin 1995; Faurobert-Scholl et al. 1995; Solanki et al. 1996; Lites et al. 1996). The best studied candidate for at least a part of this component is the so-called intranetwork field (abbreviated as IN field), composed of elements whose field strength, when averaged over a few arc seconds is on the order of 1–20 G (Livingston & Harvey 1971, 1975; Harvey 1977; Martin 1984; Livi et al. 1985; Zirin 1987; Martin 1988). IN fields are found everywhere on the quiet Sun and are seen only in particularly sensitive magnetograms. Although the physical structure of IN fields has recently been clarified to a large extent (they are either in equipartition with convection or have undergone partial convective collapse, Solanki et al. 1996, Paper XII of the present series), one important question has remained unanswered: What is the relative amount of solar surface magnetic flux in the form of intrinsically weak and strong fields?

One reason why this question is still unanswered is that high polarimetric sensitivity, i.e. very low noise in Stokes V – the difference between the two circular polarizations – and high Zeeman sensitivity, i.e. the ability to measure small intrinsic field strengths, are required simultaneously to measure the IN field strengths. In addition, a sufficiently large number of features needs to be detected in order to set meaningful limits.

Low noise observations in the Zeeman sensitive Fe I 1.5648 μm , Landé $g = 3$ line are ideal for resolving this question (with the caveat that small-scale turbulent fields cannot be detected in

this manner, since opposite magnetic polarities lying close together lead to a cancellation of the Stokes V signal). We present and discuss such observations here. They are a first attempt at using high frequency polarization modulation in the infrared in order to reduce the noise level to values below $10^{-3}I_c$. Such low noise levels are required to analyze the bulk of the IN magnetic signal reliably.

2. Observations and reduction

2.1. Observations

The quiet Sun was observed in Fe I 1.5648 μm and Fe I 1.5652 μm with the McMath-Pierce telescope, the vertical spectrograph with the new infrared grating and the Baboquivari detector (Hall 1974; Livingston 1991). The observations we analyse were mainly carried out on 11th, 15th and 16th of June 1996, although we briefly discuss some observations obtained earlier, in June 1994 and in September and November 1995. To obtain sufficiently low noise levels, we modulated the polarization at a frequency of 300 Hz using a Displaytech ferro-electric modulator. This frequency is over an order of magnitude higher than is traditionally achieved in the infrared. It is sufficiently large, so that seeing-induced noise is kept at a minimum and the high polarimetric accuracy necessary to detect IN elements is achieved. False “polarimetric” signals introduced by changes in the seeing between the 2 phases of the polarization measurement are a major source of noise in most slower modulation schemes of polarization measurement.

As detector we have used a single InSb diode, since with current technology this high modulation frequency precludes the use of an IR array detector. With this setup we have scanned the Sun at a fixed wavelength in one of the selected lines, before moving to another wavelength and scanning again. Hence we sacrifice near simultaneity of spectral information in order to cover large regions on the Sun. The main price we pay for the rapid modulation, however, is that the retardation is far from ideal. Thus, instead of measuring pure Stokes $I \pm V$ signals we obtain roughly $I \pm (V + Q)$. Consequently we need to calibrate carefully and to take this feature into account when analysing and interpreting the data.

The scans are oriented north-south, and most are approximately centred on disc centre. Six scans (those from 1995) reached from close to disc centre right up to the limb. No active region was present on the disc during the observations. A scan typically consists of 1375 samples, each corresponding to a spatial resolution of 2.38", this being the input scale from a 1×1 mm (10 elements) Bowen-type image slicer. The scanning speed was 0.4"/sec and we sampled a data point every second, so that the data are oversampled and the total length of a scan is 550". Around disc centre we obtained 15 scans for the 1.5648 μm line and 9 scans for the 1.5652 μm line, each of them corresponding to a different position in the line. The recorded wavelength position is expressed by the number of steps from an approximate determination of the line centre, which is deter-

mined with a precision of the order of the step size only (i.e., 0.053 Å).

Earlier, in 1994, we recorded scans using Beam Gate liquid crystals modulated at 10 Hz. This slow modulation has the disadvantage that seeing can introduce false signals. Therefore, we do not quantitatively analyse these data. They do have the advantage, however, that the modulation is from -90° to $+90^\circ$, so that these data are composed of pure Stokes V (except for any cross-talk from the other Stokes parameters introduced by the telescope). Therefore, by comparing qualitative properties of these data with those of the rapidly modulated measurements we can distinguish roughly between the Stokes V and Q contributions to the latter data.

2.2. Calibrations

Every two or three scans we recorded data required to calibrate for the efficiency of the polarization modulation, the dark current and the recorded wavelength. In simplified form: we obtained the difference between maximum and minimum linear Δ_l and circular Δ_c polarization signals using linear and circular polarizers. These calibration values are found to be extremely stable in time. The measured polarization values are divided by Δ_l or Δ_c . This calibration provides the polarization we would have if the signal was only circularly or only linearly polarized. We find that the actually measured signal is

$$P = \frac{1}{I} \left(\frac{Q}{\Delta_l} + \frac{V}{\Delta_c} \right) = \frac{1}{I} \left(\frac{Q}{8676} + \frac{V}{12000} \right),$$

where I is the intensity. Due to the unknown solar contribution of Q and V to the measured P , it is unclear by which factor (i.e. Δ_l or Δ_c) P should be multiplied. We have usually applied both to judge the uncertainty in the signal due to this problem.

In order to calibrate for drifts in wavelength during the observations, we record a profile of the line at wavelength steps corresponding to those at which we usually scan. This profile is used to calculate the true position of the slit for scans made just before or soon after the calibration. The wavelength turns out to be stable to within approximately 1 step (0.053 Å). This is small compared with the magnetically unbroadened line width of 0.3 Å and a Zeeman splitting of 0.7 Å produced by a 1000 G field in the $g = 3$ line (Solanki et al. 1992, Paper II of the present series). These wavelength calibration profiles also provide us with the instrumental smearing (3.6 km s^{-1}), obtained by numerically broadening profiles recorded with a narrower slit and the spectrograph in double-pass mode until they match the calibration profiles.

The September and November 1995 scans suffer from the fact that during these observing runs, the calibrations were not very reliable (only a single calibration for the line profile per run, less accurate calibrations of the polarization signal). Therefore, we restrict ourselves to a more qualitative discussion of these data.

2.3. Data reduction

We treat each scan of the data set as follows. First we remove the dark current (the signal obtained when no light enters the instrument) and then divide the Stokes polarization by the intensity (I) to obtain the fractional polarization (P). Due to the problem with the modulator pointed out in Sect. 2.1 we denote the measured polarization by P and not by V/I or Q/I . A fourth degree polynomial fit is subtracted from each scan to correct for drifts in the zero level of both P and I . Polynomials of different degrees have been tested but no significant difference in the residual rms signal is seen above the fourth degree. Since the correction of the zero level may be influenced by strong polarization peaks (or anomalous brightenings or darkenings in the case of V) we redo the correction, but this time fit only points with P or I values that differ by less than twice the rms around the first-time corrected zero level. Because the zero level we obtain after the second correction step is very similar to the first one, we stop the iteration here. We took particular care with the determination of the zero level because the value of the average or rms of the P signal is very sensitive to the zero position.

The mean brightness $\langle I \rangle$ during the scan is also calculated for the calibration of the fractional polarization. We then calibrate the slit position (given in steps from the estimated line centre).

Finally, we calculate the average of the unsigned polarization $\langle |P| \rangle$ of each scan. We calibrate the polarization using the average brightness during the scan instead of the brightness in each point of the scan. The calibration using the latter quantity provide very similar results. The center-to-limb darkening has been taken into account during the calibrations, however. The rms brightness $\langle I^2 \rangle^{1/2}$ is also calculated. It provides information on the quality of the seeing.

2.4. Sources of error in the polarization signal

The error in $\langle |P| \rangle$ contains four contributions :

- (i) The residual dark current, which should give a negligible contribution to the final signal.
- (ii) The rms signal one would obtain when observing at a fixed location on the solar disc. This noise source corresponds to photon noise and any seeing-induced noise that may not have been suppressed by the rapid modulation. We have estimated it by observing the quiet Sun at a fixed spatial location. Practically only noise contributes to the signal obtained in this way (after correcting for the zero level). This error is denoted in the following by σ_γ . We find that σ_γ is relatively independent of position in the line, suggesting that the estimate is relatively accurate.
- (iii) The statistical error due to the finite number of sampled spatial positions.
- (iv) Seeing. Although seeing is not expected to introduce any spurious polarization into the signal, it does smear out the signal and can lead to it being diluted to the extent that it is no longer detectable. Seeing can also lead to the seeming cancellation of neighbouring opposite polarities.

The most important source of *noise* is (ii), although the dominant contributors to the uncertainty in the results (Sect. 4.3) are the error sources (iii) and (iv). They must therefore be taken into account in the analysis. We estimate that σ_γ is 0.05% per pixel (linear polarization calibration). We find that this noise level does not depend on the quality of the seeing, suggesting that our modulation rate is sufficiently large to almost completely suppress seeing-induced noise. The noise can be reduced by combining the data from 4 consecutive pixels, which lie $1.6''$ apart, i.e. considerably less than the pixel size of $2.38''$. In this way the noise is reduced to $2.5 \times 10^{-4} I_c$, which is sufficient to allow us to detect average IN features.

3. Qualitative results

Reduced and calibrated scans are shown in Figs. 1 and 2. In Fig. 1 we plot full polarization scans around disc centre at 2 wavelengths in Fe I 1.5648 μm , the upper scan being close to the line core (the wavelength lies in the inner flanks of the I profile), the lower in the outer wings. The polarization near the line core obviously behaves differently from the polarization in the wings. Near the core there is significant polarization almost everywhere on the solar surface. 48% of the points have $|P| > 2\sigma_\gamma$. Far from the line core the signal is much “quieter”. There are some more or less isolated peaks separated by regions with a relatively small signal. Here only 14% of the data points show signals larger than $2\sigma_\gamma$.

Due to the large Zeeman sensitivity of this line, P in the outer wings of the I profile is produced by a sufficiently strong field ($B \gtrsim 1000$ G). Fields significantly below 1000 G give only a negligible contribution to P in the outer wings. The signal near the core obtains contributions from both weak and strong fields, however. Weak fields produce Stokes Q and V peaks in the line flanks, with significant signals in the core. The strong fields contribute to the polarization signal near the line core through two mechanisms: Firstly, due to the strong vertical gradient of the field strength in strong-field magnetic elements, these also contribute to signals near the line core (cf. Zayer et al. 1989 and Paper II). Secondly, if the strong fields are inclined relative to the line-of-sight, then we detect the π -component of their Stokes Q .

That the near-core signal is not exclusively due to strong fields is quite clear from the spatial distribution of the core and wing signals (Fig. 1), since a strong field cannot produce a core signal without a corresponding wing signal. Hence a large fraction must be due to weak fields.

An open question is whether the signal observed at the centre of the solar disc is mainly due to Stokes V or Q . We can at least qualitatively address this question using the data obtained in 1994 and 1995.

We find that scans made at different wavelengths in 1994 (with slow modulation, but measuring pure Stokes V) look very similar to those plotted in Fig. 1. This suggests that the signal in Fig. 1a (near line core) is not (or at least not dominantly) due to the Stokes Q π -component, of either strong or weak fields. This means that the strong fields are nearly vertical, since the Q

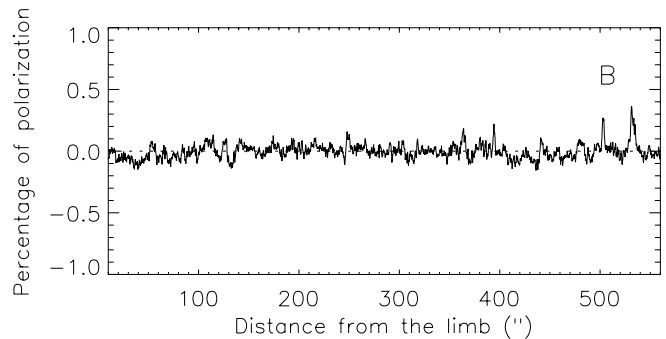
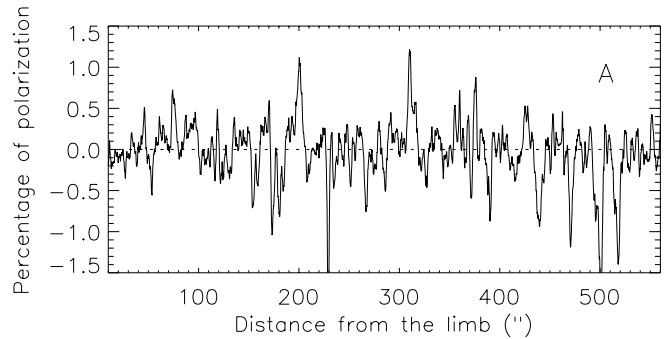
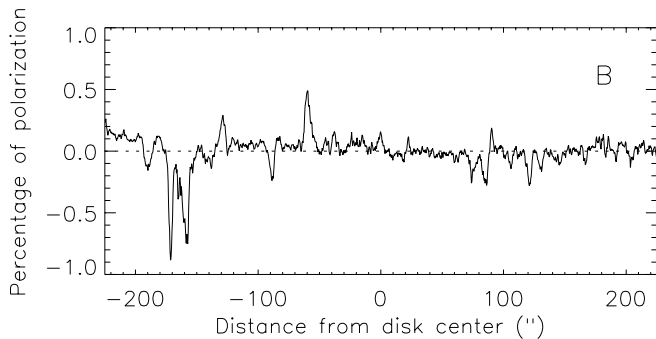
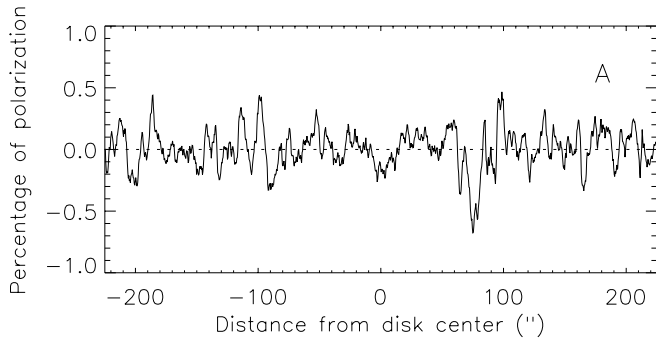


Fig. 1a and b. Two polarization scans in Fe I 1.5648 μm , one **a** close to line centre ($\Delta\lambda = 0.093 \text{ \AA}$), and the other **b** far from it ($\Delta\lambda = 0.713 \text{ \AA}$). The first scan shows mainly the signal of the ubiquitous weak fields, while the latter is only sensitive to strong kG fields, concentrated in the network. Note that almost all the structure visible in this figure is solar. The polarization scale corresponds to the linear calibration, i.e. the plotted scale is correct if the solar source is completely linearly polarized. The polarization values should be divided by 1.4 to get the correct scale in case the solar signal is mainly circularly polarized. For mixed circular and linear solar polarization, intermediate polarization levels are expected

profile of a highly inclined strong field is of the same magnitude as the V profile of a nearly vertical strong field (e.g. Paper II, Rüedi et al. 1995). The weak fields need not be vertical, however, since for them even at relatively large inclinations the Q profiles are weaker than the V (see Fig. 7 in Paper II). Lites et al. (1996) have seen a number of horizontal weak-field features in the quiet Sun, and a part of our core signal may be due to the contribution from the π -component of Q profiles. But even they cannot be the dominant source of P near the line core since the observations of Paper XII suggest that at disc centre in the quiet Sun the Stokes V amplitude is on average over 2.5 times larger than the Q amplitude.

In Fig. 2 we plot the same quantities as in Fig. 1, but now close to the limb (which lies at the left edge of the frames). Once again, the core and wing signals display a very different behaviour. Whereas P in the wing scarcely reaches values above the noise close to the limb, the core signal decreases only within less than $30''$ to the limb, if at all (in agreement with the behaviour of intranetwork fields as observed by Martin 1988). The former behaviour is typical of a field that is mainly vertical

Fig. 2a and b. Same as Fig. 1, but for scans close to the limb, which is located at the left edge of the figure. Scan **a** is at line centre, while scan **b** is at $\Delta\lambda = 0.636 \text{ \AA}$, i.e. in the outer line wings. Note that scan **a** was made during the period of best seeing of all our observations

(in agreement with Stokes vector measurements of magnetic inclination in the network, Bernasconi 1997), whereas the latter is consistent with a weak field having a distribution of inclinations, being vertical in places (giving large signals near disc centre) and nearly horizontal in others (large signals near the limb). Even for such a field we expect the signal to disappear exactly at the limb due to the combination of mixed polarities, foreshortening and our finite spatial resolution.¹

A part of the P signal near the limb may be due to Q/I near the limb produced by vertical weak fields. The small Q for even strongly inclined weak fields implies that this cannot be the main cause of P_w . However, vertical strong fields may in principle contribute significantly. Note, however, that the Q/I signal near the line core (π -component) cannot be much more than 2 times larger than in the wings (σ -components), and should slowly disappear, like the wing signal (if they were to have the same origin). Since this is not the case we conclude that at least some of the weak field features are significantly inclined (cf. Lites et al. 1996).

Note the difference in scale between Figs. 1 and 2a. The scan plotted in Fig. 2a was obtained under the conditions of the best seeing of all our observations, and also has the largest polarization. This greatly supports the idea that the weak-field

¹ The generally small signals seen in Fig. 2b are due to the comparatively poor seeing present during the recording of the plotted scan.

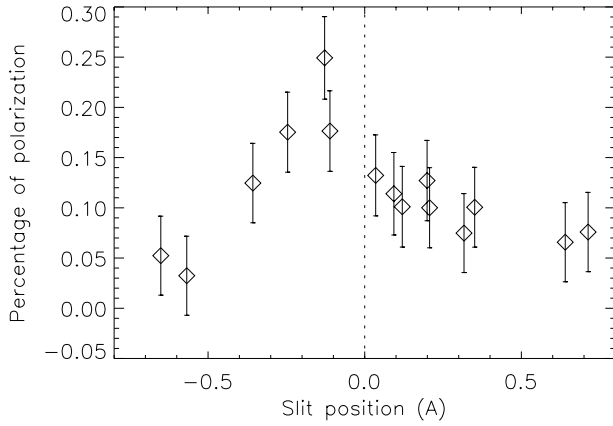


Fig. 3. Polarization “profile” $\langle |P| \rangle (\lambda)$ of the 1.5648 μm line, where $\langle |P| \rangle$ is the unsigned polarization averaged over a whole scan. Error bars are at the 1- σ level and take into account both photon noise and statistical errors due to the finite number of points

magnetic features are spatially unresolved, in agreement with Paper XII.

4. The relative flux in weak and strong fields

4.1. The observational input

In this section, we present an analysis aimed at determining the ratio of flux contained in weak fields relative to strong fields. To this end we use the average of the unsigned polarization $\langle |P| \rangle$ at each wavelength in the lines 1.5648 μm and 1.5652 μm . An example of the resulting statistical “line profile” is shown in Fig. 3. To increase the signal-to-noise ratio for the further analysis, we calculate the average of $\langle |P| \rangle$ for wavelengths far from line centre, i.e. $|\Delta\lambda|$ in the range 0.5–0.7 \AA (we call this averaged signal P_s , since it provides information mainly on strong fields; Sect. 3) and close to line centre, i.e. for $|\Delta\lambda|$ in the range 0.1–0.5 \AA (P_w , significant information on weak fields). $|\Delta\lambda|$ is the wavelength difference from line centre. Then we compute the ratio between the polarization close to the line core and far from it (P_w/P_s).

More precisely, the polarization far from the line core really is mainly due to strong fields, while close to the core it is due to both weak and strong fields (Sect. 3). Nevertheless, our observations and our knowledge of magnetic elements allow us to constrain the contribution of strong fields to the polarization signal near the line core. A model fitting the ratio P_w/P_s can thus provide an estimate of the relative amounts of flux in weak and strong fields, respectively.

The following sources contribute to the relative uncertainty of the observed P_w/P_s .

(i) The relative uncertainties in P_w and P_s are respectively $\sigma_w = 0.017\%$ and $\sigma_s = 0.025\%$ (for the linear calibration, 1.5648 μm line). Note that σ_w and σ_s include the statistical error due to the finite length of our scans.

(ii) The strong field also contributes to P_w . This effect is taken fully into account in the modelling, and need not be considered here further.

(iii) Any changes in the spatial resolution between the different scans can also influence the P_w/P_s ratio.

While we can easily estimate or compensate for the influence of points (i) and (ii), that of point (iii) is more difficult to judge. By modulating quickly we have been able to remove the first order influence of seeing on our observations, but the second order influence, namely that different scans may have been made under situations with different seeing, cannot be so easily dealt with. If, for example, the scans made closer to line centre had better seeing, then we would overestimate the fraction of flux in weak-field form. In the opposite case we would underestimate this quantity.

Neglecting the influence of point (iii) for the moment, the minimum and maximum of the ratio P_w/P_s is

$$\left(\frac{P_w}{P_s} \right)_{\text{max,min}} = \frac{P_w}{P_s} \left(1 \pm \sqrt{\left(\frac{\sigma_w}{P_w} \right)^2 + \left(\frac{\sigma_s}{P_s} \right)^2} \right).$$

P_w and P_s are the fractional polarizations defined above (close to line centre and far from it), while σ_w and σ_s are the respective uncertainties in these average polarizations (point (i) above). Our observations give us $(P_w/P_s)_{\text{min}} = 1.5$ and $(P_w/P_s)_{\text{max}} = 3.5$, with an average ratio of approximately 2.5. Both, the ratio itself and the error bars, i.e. the quantity in the large brackets on the RHS, are independent of whether we use the linear or the circular calibration.

Let us now return to uncertainty (iii). One way of estimating the seeing is to consider the rms of Stokes I , which is measured simultaneously. We plot this as a function of relative wavelength in Fig. 4. As one can see, the rms is larger at the centre of the line. This could be because the seeing was indeed better during the periods at which the wavelengths near the centre of the line were observed. On the other hand, fluctuations in I probably are larger in the core of this spectral line, since it weakens when the temperature is raised (cf. Paper II), so that the intensity enhancement in the core is due to both the continuum enhancement and the line weakening. In addition, velocity shifts (due to granulation) lead to spatial intensity fluctuations, particularly in the line flanks. Finally, we expect a slightly higher relative rms in the line core simply due to the lower signal there (noise).

In order to obtain a strict lower limit on the amount of weak-field flux we take the conservative stance that the whole increase in $I_{\text{rms}}/\langle I \rangle$ towards line centre is entirely due to changes in seeing. We then smear the I and P scans having larger rms of I until the I_{rms} values are the same for all the scans. After this procedure, we repeat our whole analysis. The resulting ratios between the inner and outer parts of the $\langle |P| \rangle$ profile are: $(P_w/P_s)_{\text{min}} = 1.3$, $(P_w/P_s)_{\text{max}} = 2.5$, with an average ratio of 1.9.

For the 1.5652 μm line, the error bars on the ratio, 4.85, are unfortunately too large, so that the constraints cannot be

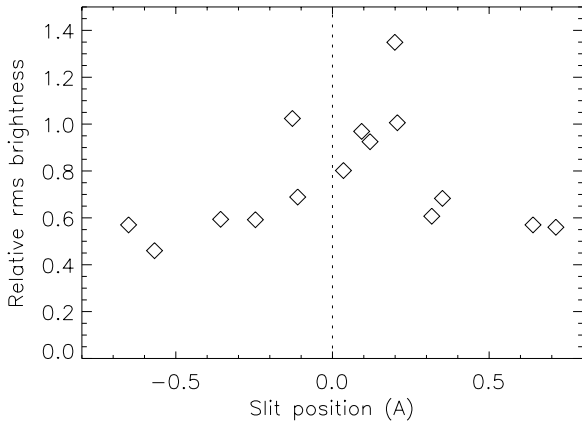


Fig. 4. Relative rms, $I_{\text{rms}}/\langle I \rangle$, of the intensity versus slit position in the 1.5648 μm line

sharpened by using this line in addition to the 1.5648 μm line. We find in the following that the observed P_w/P_s of this line is consistent with that of $\lambda 1.5648 \mu\text{m}$, in the sense that the model reproducing the latter also reproduces the former.

4.2. The model

We compare the observational data with synthetic profiles. These are calculated using flux-tube models similar to those used in Paper XII. A single magnetic component with a field strength typical of network fields ($B(z=0) = 1500 \text{ G}$) cannot reproduce the observations, as expected already by considering Fig. 1, which shows that the magnetic signal near the line core is distributed in elements that are separated by much smaller distances than the signal far from line centre.

We need a combination of two magnetic components, an intrinsically strong (subscript s) and a weak field (subscript w):

(i) *The strong field.* The properties of the strong-field component representing the network are well known: $B_s(z=0) = 1500 \text{ G}$, the inclination $\langle \gamma_s \rangle \approx 10^\circ$ (this takes into account the average inclination to the vertical of network elements found by Bernasconi 1997, as well as the average inclination to the line-of-sight introduced by the length of the scan and the curvature of the Sun). The thermal model corresponds to the network flux-tube model of Solanki & Brigljević (1992).

(ii) *The weak field.* The parameters of the weak field are less reliably known. Of the three magnetic parameters, the intrinsic strength of the weak field B_w , the mean inclination of weak fields $\langle \gamma_w \rangle$ and the fraction of flux contained in weak-field structures

$$F_w = \frac{\Phi_w}{\Phi_{\text{tot}}} = \frac{\Phi_w}{\Phi_w + \Phi_s},$$

we find estimates for the first two and treat the third as the free parameter of the model. For the temperature of the weak-field features, we take the quiet-sun stratification. Due to the low temperature sensitivity of the infrared lines, this choice is relatively uncritical. We estimate that the relative error introduced into

the analysis by possibly incorrect choices of the temperatures of both strong- and weak-field elements is less than 20%.

The F_w we obtain depends on the choice of B_w , since V_w and Q_w scale with B_w , respectively B_w^2 , so that in order to reproduce the observations a larger F_w is required if a smaller B_w is chosen. The results of Paper XII suggest that $200 \text{ G} \leq B_w(z=0) \leq 800 \text{ G}$. Our observations do not allow us to distinguish between these B_w values. In the following we shall therefore derive F_w for both $B_w = 200 \text{ G}$ and 800 G .

Unfortunately, the constraints on γ_w are even weaker. Its choice also affects the resulting $F_w = \Phi_w/\Phi_{\text{tot}}$, since at $B_w \leq 800 \text{ G}$ the synthetic signal is larger for $\gamma_w \approx 0$ (basically V_w/Δ_c in this case) than for $\gamma_w \approx 90^\circ$ (basically Q_w/Δ_l). This is because at low field strengths the intrinsic strength of $V(\gamma=0) \gg Q(\gamma=90^\circ)$, outweighing the lower modulator efficiency for V .

As pointed out in Sect. 3, the inclination of weak-field flux tubes is necessary to explain the large signal near the line core at small μ . The P_w/P_s ratio is sensitive to this inclination, so we have to take it into account. We estimate that the *average* inclination to the vertical of weak fields is smaller than 70° . This limit is set by the observation described in Paper XII that at disc centre on average $V > 2.5Q$.

Note that we weight the synthetic V and Q profiles in exactly the same manner as the observed circular and linear polarizations are weighted by the modulator; i.e. we multiply the synthetic Q profile by the ratio $\Delta_l/\Delta_c = 1.38$ before adding the profiles together. We also take the instrumental spectral smearing into account by convolving the calculated profiles with the corresponding Gaussian.

We now search for models that reproduce the minimum, maximum and average ratios. We use models with different B_w and γ_w . By considering these parameters in a reasonable range of values we can set upper and lower limits on the relative amounts of flux in weak and strong field form.

4.3. Results

The results of a selected sample of fits are given in Table 1. These fits correspond to P_w/P_s values that have not been changed to correct for possible seeing differences between scans. We have listed those fits with extreme values of B_w and γ_w , since these delineate the smallest and largest fractions of weak-field flux that we obtain.² We also present in the last line of Table 1 the results of a model with a mixture of weak and strong, vertical and inclined fields. It has an equal amount of flux in each of the four types of weak fields: a vertical 200 G, a horizontal 200 G, a vertical 800 G and a horizontal 800 G field. The observations described in Sect. 3 suggest that the weak field has a range of inclinations, with almost the same amount of flux in vertical as in horizontal fields. Such a range of orientations is also suggested by the good visibility of intranetwork fields at all limb distances

² Note that what we call the flux is actually the spatially averaged field strength. For a given spatially averaged field strength the flux perpendicular to the solar surface is, of course, smaller in the case of an inclined field compared to a vertical field.

Table 1. Relative flux in weak-field form. Original P_w/P_s

B_w G	γ_w °	$F_{w,\min}$ %	$F_{w,\max}$ %	$F_{w,\text{avge}}$ %
200	0	30	71	56
200	70	40	84	70
800	0	37	80	64
800	70	42	86	71
mixed	mixed	38	83	70

Table 2. Relative flux in weak-field form. P_w/P_s changed to take into account possible seeing variations

B_w G	γ_w °	$F_{w,\min}$ %	$F_{w,\max}$ %	$F_{w,\text{avge}}$ %
mixed	mixed	25	70	55

in the magnetograms of Martin (1988). In addition, the observations of Lin (1995) and in particular those of Solanki et al. (1996, Paper XII) indicate that all field strengths between 200 and 800 G are represented in typical intranetwork fields.

Table 1 tells us that the main uncertainty (approximately a factor of 2) in the fraction of the weak-field flux (F_w) comes from the uncertainty in the observations, and not from any uncertainty in the parameters of the weak field entering the model (i.e. mainly B_w and γ_w), which together provide only approximately 20% uncertainty. Note that this uncertainty is actually even smaller, since the observations plotted in Fig. 2a clearly show that the weak field cannot be purely vertical, but must have a highly inclined component as well. Hence, the models with $\gamma_w = 0$ listed in Table 1 are not realistic. They only serve to illustrate the influence of γ_w on the relative flux.

In Table 2 those F_w values are given, which satisfy the P_w/P_s ratios after the scans have been smeared in such a way that the rms of I is the same for all. Only the F_w obtained with the most realistic model are listed. As expected, the fraction of flux in weak-field form is now considerably lower. Note, however, that in this manner we have probably overestimated the influence of seeing (see Sect. 4.1).

The average value of F_w we find is somewhat smaller than in Paper XII, although the two values agree within the error bars. Since a part of the difference may have to do with the way that flux is determined, we have investigated the possible influence of an assumption which is different in the two investigations. Whereas in Paper XII we assumed that the area covered by a magnetic feature is circular, here we have taken it to be rectangular, with the width of the rectangle being the pixel size. If we redo our analysis under the same conditions as that underlying Paper XII we find an average F_w of 76%, with minimum and maximum values of 60% and 86%, respectively (no correction was made for differential seeing). Except for the lower limit on F_w the values are not excessively influenced by the way an apparent area is assigned to each magnetic feature. For comparison, the value F_w in Paper XII was roughly 80%.

In summary, we can say that between 25 and 85% of the total magnetic flux in the quiet solar photosphere is in weak-

field form (i.e. lower than 1000 G), with the most likely value being around 65%. To some extent these estimates are affected by the limited sampling (which gives rise to the major part of the uncertainty).

5. Further results

5.1. Typical distance between magnetic features

In this section we calculate the average distance between magnetic features. We only consider polarization peaks whose *average* polarization is above 0.05%, where a peak is defined as the region between two zero-crossings.

The average distance between such peaks is calculated for scans with $|\Delta\lambda| < 0.5 \text{ \AA}$. We obtain an average distance between peaks of $9.4 \pm 0.5''$. This distance also supports the identification of the weak-field features with intranetwork elements. We find no obvious correlations with brightness fluctuations.

We also measured the average distance between the strong-field features, i.e. the distance between the significant peaks on scans far from the line core. We find a typical distance of $50''$. These strong-field features are probably network elements. Note that since our observations consist of 1-D scans, we do not expect the scan to cross a network magnetic element each time it crosses a supergranular cell boundary (i.e. every 20–30''). A correlation between these features and bright structures in the I scans is observed.

5.2. Spatial power spectra

The scans also makes possible the study of the turbulence properties of the weak-field features, as revealed by their distribution on the Sun. For this purpose, we have calculated the power spectra of the polarization scans at three positions in the $1.5648 \mu\text{m}$ line. An example of such a power spectrum is shown in Fig. 5. The plot of these power spectra on a logarithmic scale exhibits two slopes, a flatter slope at scales larger than 10–20'' and a steeper slope at smaller scales down to $2.4''$ (i.e. the size of the entrance aperture). Close to line centre (i.e. where most of the observed features are weak-field features), we obtain slopes of -0.41 ± 0.01 at large scales and -1.74 ± 0.02 at small scales. For scans further from line centre (where the weak-field component gives a smaller contribution), the absolute value of the slope at small scales is significantly smaller (-1.43 ± 0.02 at 0.318 \AA and -1.37 ± 0.02 at 0.632 \AA), as well as at large scales (-0.25).

The absolute values of these slopes are larger than those found by Lee et al. (1997) at similar scales. This may have to do with the fact that they spatially deconvolved their data and thus had better spatial resolution (and smaller pixel size). Lower spatial resolution tends to give steeper drops in the power towards higher spatial frequencies. The difference between the slopes found for weak and strong fields should, however, not be an artifact of any differences in spatial resolution during measurements close to or far from line centre. As Fig. 4 shows the spatial resolution was certainly not worse during the observa-

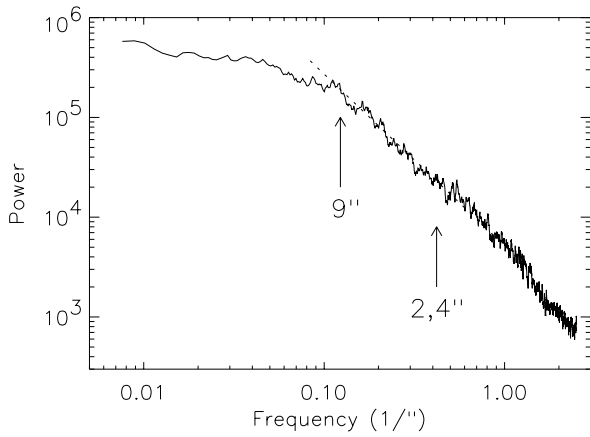


Fig. 5. Average of the spatial power spectra of two polarization scans close to line centre ($1.5648 \mu\text{m}$), plotted on a logarithmic scale

tions near line centre than during the observations carried out in the line wings. If anything, it was better.

5.3. Distribution of flux

We have also determined the flux distribution of the magnetic features. The flux of each feature is determined using our radiative transfer calculations to convert from P into average field strength, under the two following assumptions: (i) the dimension of the features in the direction perpendicular to the scan is given by the pixel size; (ii) the distance between two zero crossings of the signal represents the diameter of a magnetic feature (whereby the overlap between pixels is taken into account).

We have also repeated our analysis assuming circular features, and have obtained very similar results. Hence the results depend only slightly on assumption (i). Assumption (ii) is more severe. In the original scans there often is more than a single peak between 2 zero crossings, suggesting that due to our assumption (ii) many “features” are composites of individual solar magnetic features. Also, what appears as a single magnetic feature in our scans may well be composed of numerous unresolved “flux tubes”. Therefore, we are overestimating the flux per feature. Finally, the conversion factors from fractional polarization into Gauss also suffer from some uncertainty. For $|\Delta\lambda| < 0.5 \text{ \AA}$ we find for intrinsically weak fields that on average 1 G corresponds to $P = 2.5\text{--}5 \times 10^{-4}$, although this value depends on the wavelength, the temperature, and the strength and inclination of the field. For network fields a similar P corresponds to approximately 5 G, mainly due to the larger field strength (note that due to the large Zeeman sensitivity of the $g = 3$ line, its P amplitude saturates already at relatively low field strengths). Another uncertainty is due to the fact that our calibration for $\Delta\lambda < 0.5 \text{ \AA}$ assumes that all fields are intrinsically weak, although we know from our radiative transfer calculations that intrinsically strong fields also contribute to the signal. For such signals in the $|\Delta\lambda| < 0.5 \text{ \AA}$ scans the chosen calibration results in a too small flux.

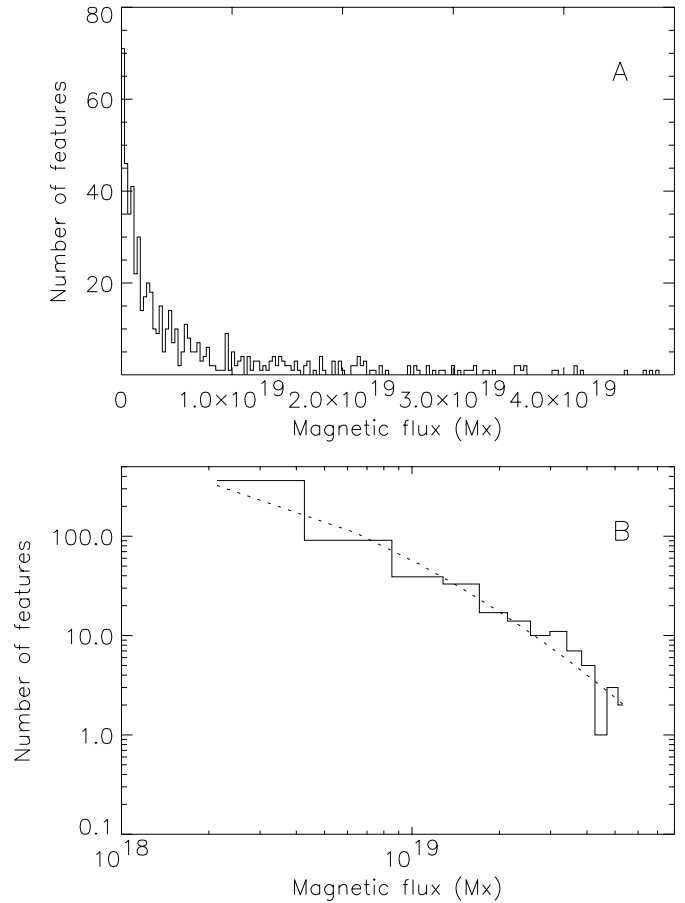


Fig. 6. **a** Histogram of unsigned magnetic flux derived from scans with $|\Delta\lambda| < 0.5 \text{ \AA}$ ($1.5648 \mu\text{m}$ line), i.e. scans preferentially showing the signature of intrinsically weak solar fields. **b** Same as **a**, but as a log-log plot with wider bins. The dotted curve is the best-fit lognormal distribution.

We select features whose polarization averaged over all points between two zero-crossings is above σ_γ . Since each feature consists of a number of pixels, typically 4 or more, its flux is significant at above the 2σ -level. To increase the number of points per bin, we consider in the following the distribution of the absolute value of the flux. The flux distribution resulting from all scans with $|\Delta\lambda| < 0.5 \text{ \AA}$ is shown in Fig. 6. It represents a mixture of weak- and strong-field features. Note the presence of the strong and narrow peak at small fluxes and the long tail of high-flux features.

It is not possible to adequately fit the plotted distribution with one or two Gaussians, due to the prominent tail of high-flux features. However, fits based on a lognormal distribution reproduce the observed flux distribution quite well, as shown in Fig. 6b for $|\Delta\lambda| < 0.5 \text{ \AA}$ and in Fig. 7 for $|\Delta\lambda| > 0.5 \text{ \AA}$.

From the weak-field flux distribution, we determine a median flux per feature of $2.7 \cdot 10^{18} \text{ Mx}$. The lognormal distribution provides a width of approximately $9 \cdot 10^{17} \text{ Mx}$. In the case of the distribution obtained from scans far from line center, i.e. for

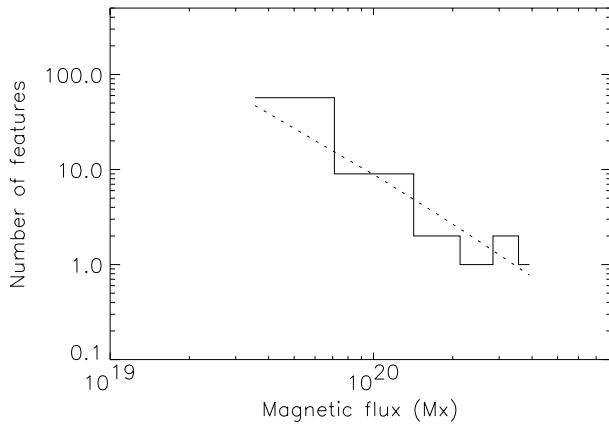


Fig. 7. Histogram of unsigned magnetic flux derived from scans with $|\Delta\lambda| > 0.5 \text{ \AA}$ (1.5648 μm line), as a log-log plot. The dotted curve is a fit involving a lognormal distribution.

purely strong-field features, the parameters of the fit are not very reliable due to the much smaller number of features in these scans. The flux distribution we find implies that the logarithm of the flux per magnetic feature is normally distributed. Note that sunspot umbral areas are also distributed lognormally (Bogdan et al. 1988), while it is not the case for more complex structures such as active regions. A lognormal distribution is often related to fragmentation processes.

The strong-field features (network fields) also contribute to the signal near the line core. To obtain a better estimate of the distribution of weak flux alone we subtract from the histogram in Fig. 6 the scaled lognormal fit to the strong field histogram shown in Fig. 7: the amplitude has been multiplied by a factor of 2.66, which is the ratio of the total length of the scans at small $|\Delta\lambda|$ relative to the total length at large $|\Delta\lambda|$, and the width has been divided by a factor of 5, which comes from the different flux calibration for weak and strong fields. The resulting distribution is plotted in Fig. 8. It is very similar to that shown in Fig. 6. The parameters of the lognormal fit are also almost the same, although the slope is then slightly steeper. We obtain higher magnetic fluxes per features than observed by Wang et al. (1995). This could be explained by the contribution of several individual features to each of our observed features. They also observe a much steeper slope of the distribution.

5.4. Asymmetry of the polarization profile

We now study the asymmetry of the polarization profile. We calculate $\langle |P| \rangle$ for each spectral position in the lines 1.5648 μm and 1.5652 μm , using three selections of points from the scans:

- (A) all the points;
- (B) points with polarization smaller than $2P_{\text{rms}}$;
- (C) points with polarization higher than $2P_{\text{rms}}$.

In order to lower the influence of noise, we average the results over the following wavelength ranges: -0.7 to -0.5 \AA (P_1); -0.5 to -0.1 \AA (P_2); 0.1 to 0.5 \AA (P_3); 0.5 to 0.7 \AA

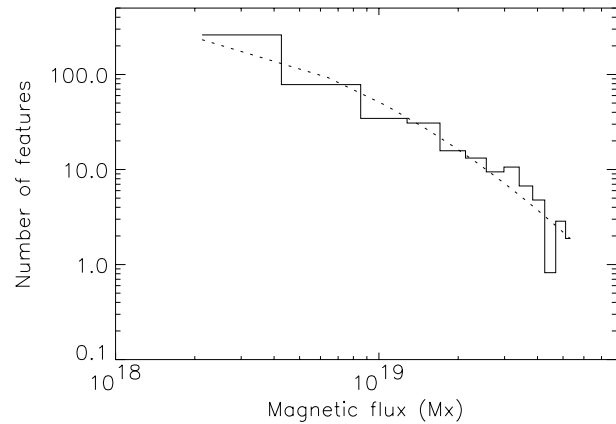


Fig. 8. Flux histogram of intrinsically weak magnetic fields, i.e. a histogram of unsigned magnetic flux derived from scans with $|\Delta\lambda| < 0.5 \text{ \AA}$ (1.5648 μm line), after removal of the intrinsically strong field distribution (see text), as a log-log plot. The dotted curve is a fit involving a lognormal distribution.

(P_4). From this we calculate the asymmetry of the profile far from the line core $A_s = (P_1 - P_4)/(P_4 + P_1)$ and close to it $A_w = (P_2 - P_3)/(P_3 + P_2)$, for the three selections A, B, and C. The results are listed in Table 3. The observed asymmetry of Fe I 1.5648 μm fits in quite well with the picture of how the asymmetry is produced. The inner part of the spectral line, which is associated mainly with weak fields, exhibits a sizable asymmetry of over 20% at the $2-4\sigma$ level, whereas the outer parts of the line show no asymmetry significantly above the noise (in agreement with the theoretical expectations outlined by Grossmann-Doerth et al. 1989).

The value for the 1.5652 μm line are not significant (due to the fewer points) and have consequently not been tabulated.

Since we do not measure all the wavelengths in the line profile simultaneously, it cannot be *a priori* ruled out that the asymmetry is an artifact of different seeing for the different scans. Of importance is only, whether the seeing was similar on the blue and the red sides of the profile, and not how strongly it varied with distance from the line core.

To test this we have also determined the asymmetry after smearing the scans with large I_{rms} as described in Sect. 4.1. Only A_w is affected by this procedure. We denote the asymmetry after smearing by A_w^* and list it in the last column of Table 3. The A_w^* values confirm that the Stokes profiles of weak-field features are on average significantly asymmetric, although the exact relation of A_w to the well-known Stokes V area asymmetry (Solanki & Stenflo 1984) is not entirely clear. We must warn that an average asymmetry in our data does not necessarily imply asymmetric Stokes V or Q profiles of individual magnetic features. For example a correlation between line shift and splitting can produce a seeming asymmetry, when many “spectral profiles” are averaged.

Table 3. Asymmetry of the polarization profile, for different selections of points (see text)

selection	A_s	A_w	A_w^*
15648 (A)	-0.22 ± 0.21	0.29 ± 0.14	0.34 ± 0.14
15648 (B)	-0.31 ± 0.29	0.27 ± 0.16	0.35 ± 0.14
15648 (C)	0.002 ± 0.06	0.25 ± 0.06	0.31 ± 0.06

6. Conclusion

From low noise observations made at $1.56 \mu\text{m}$ in the infrared we find that between 25 and 85% of the flux in the quiet Sun is in the form of intrinsically weak fields (i.e. with intrinsic field strengths below 1000 G in the lower photosphere).

Over the years an ever wider variety of techniques has been used in an attempt to set limits on the flux in weak-field form. Thus Stenflo (1982), Faurobert-Scholl (1993), Faurobert-Scholl et al. (1995) and Stenflo et al. (1997) have determined the average flux in the form of field. They find average field strengths on the order of 10 G. This type of intrinsically weak field that is turbulent on a small scale is not expected to be what we observe.

The features we see have a flux per feature of around 10^{18} Mx. Many (but by far not all) of them are relatively well separated in our observations, properties reminiscent of the intranetwork field. Of course, our field may be simply the large wavelength limit of the turbulent background field. The intrinsic field-strengths measured by Lin (1995) and in Paper XII, however, speak against this interpretation. The intranetwork fields have strengths that are in equipartition with convective motions or are even larger, suggestive of flux tubes that have undergone partial convective collapse. They may, however, be related in origin to a truly turbulent field in that they are created by a small-scale dynamo, as proposed by Petrovay & Szakaly (1993) and Durney et al. (1993). The presence of such a turbulent convection-zone dynamo has also been proposed in connection with the modelling of Maunder-Minimum like states (Schmitt et al. 1996, cf. Nordlund et al. 1992). The typical flux per feature is higher in this study than in previous ones (Wang et al. 1995). One explanation could be that we are less sensitive to the smallest features. In such a case, the actual ratio between weak and strong fields could be higher than the ratio obtained in Sect. 4.

Although the large fraction of flux in the form of intrinsically weak fields is in good agreement with a previous such estimate based on infrared lines (Paper XII), it disagrees with the estimate of Frazier & Stenflo (1972), Howard & Stenflo (1972) and Stenflo (1973) that over 90% of the flux visible in magnetograms is in the form of kG fields, which was based on longitudinal multi-line magnetograms in the visible. The reason for the discrepancy is probably the insufficient sensitivity of their data to small magnetic fluxes.

The relative amounts of flux in weak and strong fields is also similar to the relative amounts of flux in intranetwork and network fields deduced by Wang et al. (1995). They find that at least 20% of the flux at any given time is in the form of intranetwork fields. This again supports the idea that we are

mainly measuring intranetwork fields. The larger amounts of relative flux which we find and was also found in Paper XII, may have to do with the higher sensitivity of the $1.5648 \mu\text{m}$ line to intrinsically weak fields than the visible lines used by Wang et al. (1995). The weak horizontal and transient fields detected and discussed by Lites et al. (1996) may also be contributing to our signal, in particular near the limb.

We also find that the flux distribution of the quiet-sun magnetic features is best described by a lognormal function, in qualitative agreement with the distribution of sunspot umbral areas found by Bogdan et al. (1988). Since the spatially averaged magnetic field strength of sunspots is expected to be roughly independent of their size (Solanki & Schmidt 1993), the result of Bogdan et al. implies that the magnetic flux of sunspots is also lognormally distributed. Hence the flux of both the smallest and largest known magnetic features shows the same type of distribution. Lognormally distributed quantities are often the result of fragmentation processes. The common type of flux distribution may imply a common origin of sunspot and intranetwork magnetic features. However, our result mainly highlights the need for further work on this topic.

Acknowledgements. We are grateful to E. Nesme-Ribes for fruitful discussions and to J.W. Harvey for his helpful comments on the manuscript.

References

- Bernasconi P., 1997, Ph. D. Thesis, ETH Zürich
 Bogdan T.J., Gilman P.A., Lerche I., Howard R., 1997, A&A 327, 451
 Durney B.R., De Young D.S., Roxburgh I.W., 1993, Sol. Phys. 145, 207
 Faurobert-Scholl M., 1993, A&A 268, 765
 Faurobert-Scholl M., Feautrier N., Machefer F., Petrovay K., Spielfiedel A., 1995, A&A 298, 289
 Frazier E.N., Stenflo J.O., 1972, Sol. Phys. 27, 330
 Grossmann-Doerth U., Schüssler M., Solanki S.K., 1989, A&A 221, 338
 Hall D.N.B., 1974, An Atlas of Infrared Spectra of the Solar Photosphere and of Sunspot Umbrae, Kitt Peak National Observatory, Contribution No. 556, Tucson, AZ.
 Harvey J.W., 1977, in Highlights of Astronomy, E.A. Müller (Ed.), Vol. 4, p. 223
 Howard R.F., Stenflo J.O., 1972, Sol. Phys. 22, 402
 Keller C.U., Deubner F.L., Egger U., Fleck B., Povel H.P. 1994, A&A 286, 626
 Lee J., Chae J.-C., Yun H.S., Zirin H., 1997, Sol. Phys. 171, 269
 Lin H., 1995, ApJ 446, 421
 Lites B.W., Leka K.D., Skumanich A., Martínez Pillet V., Shimizu T., 1996, ApJ 460, 1019
 Livi S.H.B., Wang J., Martin S.F., 1985, Australian J. Phys. 38, 855
 Livingston W.C., 1991, in: Solar Polarimetry, L. November ed., NSO, Sunspot, NM, 356
 Livingston W., Harvey J.W., 1971, in Solar Magnetic Fields, R. Howard (Ed.), Reidel, Dordrecht, IAU Symp. 43, 51
 Livingston W., Harvey J.W., 1975, BAAS 7, 346.

- Martin S.F., 1984, in *Small-Scale Dynamical Processes in Quiet Stellar Atmospheres*, S.L. Keil (Ed.), National Solar Obs., Sunspot, NM, p. 30
- Martin S.F., 1988, *Sol Phys* 117, 243
- Nordlund Å., Brandenburg A., Jennings R.L., Rieutord I., 1992, *A&A* 265, 843
- Petrovay K., Szakaly G., 1993, *A&A* 274, 543
- Rüedi I., Solanki S.K., Livingston W., Stenflo, J.O., 1992, *A&A* 263, 323 (Paper III)
- Rüedi I., Solanki S.K., Livingston W., Harvey J.W., 1995, *A&AS* 113, 91
- Schmitt D., Schüssler M., Ferriz Mas A., 1996, *A&A* 311, L1
- Solanki S.K., 1993, *Space Sci. Rev.* 61, 1
- Solanki S.K., Brigljević V., 1992, *A&A* 262, L29
- Solanki S.K., Schmidt H.U., 1993, *A&A* 267, 287
- Solanki S.K., Stenflo J.O., 1984, *A&A* 140, 185
- Solanki S.K., Rüedi I., Livingston W., 1992, *A&A* 263, 312 (Paper II)
- Solanki S.K., Zuffrey D., Lin H., Rüedi I., Kuhn J., 1996, *A&A* 310, L33 (Paper XII)
- Spruit H.C., Roberts, B., 1983, *Nat.* 304, 401
- Stenflo J.O., 1973, *Sol. Phys.* 32, 41
- Stenflo J.O., 1982, *Sol. Phys.* 80, 209
- Stenflo J.O., 1989, *A&A* 210, 403
- Stenflo J.O., 1994, *Solar Magnetic Fields: Polarized Radiation Diagnostics*, Kluwer, Dordrecht
- Stenflo J.O., Keller C.U., Gandorfer A., 1997, *A&A* submitted
- Tarbell T.D., Title A.M., Schoolman S.A., 1979, *ApJ* 229, 387
- Thomas J.H., Weiss N., (Eds.) 1992, *Sunspots: Theory and Observations*, Kluwer, Dordrecht
- Wang J., Wang H., Tang F., Lee J.W., Zirin H., 1995, *Sol. Phys.* 160, 277
- Zayer I., Solanki S.K., Stenflo J.O., 1989, *A&A* 211, 463
- Zirin H., 1987, *Sol. Phys.* 110, 101